ADVANCED PHOTONICS RESEARCH
Open Access
www.adpr-journal.com

# Active Chiral Plasmonics: Flexoelectric Control of Nanoscale Chirality

*Cameron Gilroy, Katie McKay, Machar Devine, Robert W. H. Webster, Nikolaj Gadegaard, Affar S. Karimullah, Donald A. Maclaren,* and Malcolm Kadodwala**

**The ability to electrically control the optical properties of metamaterials is an essential capability required for technological innovation. The creation of dynamic electrically tunable metamaterials in the visible and near infrared regions is important for a range of imaging and fiber optic technologies. However, current approaches require complex nanofabrication processes which are incompatible for low-cost device production. Herein, a novel simple approach is reported for electrical control of optical properties which uses a flexoelectric dielectric element to electromechanically manipulate the form factor of a chiral nanostructure. By altering the dimensions of the chiral nanostructure, the polarization properties of light are allowed to be electrically controlled. The flexoelectric element is part of a composite metafilm that is templated onto a nanostructured polymer substrate. As the flexoelectric element does not require in situ high temperature annealing, it can be readily combined with polymer-based substrates produced by high throughput methods. This is not the case for piezoelectric elements, routinely used in microelectromechanical (MEM) devices which require high temperature processing. Consequently, combining amorphous flexoelectric dielectrics and low-cost polymer-based materials provides a route to the high throughput production of electrically responsive disposable metadevices.**

## 1. Introduction

Metamaterials formed from nanofabricated subwavelength-sized elements have had a disruptive influence in the field of optics, providing new ways of manipulating and exploiting electromagnetic (EM) fields.[1] The earliest metamaterials were passive elements with optical properties that were predetermined by structure design, materials, and dielectric environments. An important area of innovation is the development of new concepts for "dynamic" metamaterials, for which optical properties can be actively controlled by external stimuli.[2–6] Active control in the visible and near infrared (NIR) regions is a requirement for developing novel imaging and optical processing technologies. Currently, dynamic tuning in this region is achieved either by altering the dielectric environment or by manipulating the physical structure of the metamaterial.[4,7–16] These established strategies suffer from two principle weaknesses: they either require complex nanofabrication procedures that are incompatible with high throughput, low-cost production, or they do not rely on electrical stimuli. Dynamic manipulation of properties using, for example, heat, magnetism, or light is less desirable than electrical control for device implementation.

Piezoelectric ceramic materials are routinely used to create micro (nano) electromechanical (M(N)EM) devices.[17] However, they require in situ high temperature processing which is incompatible with polymer platforms that are fabricated by high throughput processes such as nanoimprint[18] and injection moulding.[19]

The piezoelectric effect is the spontaneous creation of a dipole moment in some materials by the application of pressure. Conversely, the inverse piezoelectric effect describes the generation of stress (i.e., a change in volume) by the application of an electric field. The effect occurs in crystalline materials without inversion symmetry, typically ceramics with perovskite structures.[20] A problem is that low temperature deposition methods for piezoelectric materials including $Pb(Zr_xTi_{1-x})O_3$ (PZT) onto amorphous substrates typically produce amorphous films that require annealing to temperatures significantly beyond the softening point of polymers before they crystallize and display piezoelectric effects.[21] Thus, there are significant hurdles

C. Gilroy, K. McKay, M. Devine, Dr. A. S. Karimullah, Prof. M. Kadodwala
School of Chemistry
University of Glasgow
Glasgow G12 8QQ, UK
E-mail: malcolm.kadodwala@glasgow.ac.uk

Dr. R. W. H. Webster, Dr. D. A. Maclaren
SUPA, School of Physics and Astronomy
University of Glasgow
Glasgow G12 8QQ, UK
E-mail: donald.maclaren@glasgow.ac.uk

Prof. N. Gadegaard
School of Engineering
Rankine Building
University of Glasgow
Glasgow G12 8LT, UK

The ORCID identification number(s) for the author(s) of this article can be found under https://doi.org/10.1002/adpr.202000062.



**DOI: 10.1002/adpr.202000062**

in creating polymer-based platforms that incorporate piezoelectric elements.

Herein, we demonstrate a polymer-based nanoelectromechanical metamaterial which provides dynamic control of the polarization of light by manipulating the dimensions of nanoscale chiral elements. The composite metamaterial consists of an array of chiral nanostructured indentations in a polycarbonate substrate which have previously been shown to exhibit large chiroptical effects.[19] The polycarbonate is then overlaid by a sandwiched metafilm, which contains a layer (50/150 nm) of amorphous PZT. The intrinsically weak electromechanical response of amorphous PZT is amplified by flexoelectric effects, which are significant because of the large electrostatic field gradients generated by the nanostructured film. Consequently, we demonstrate a strategy to create NEM devices without the need for high temperature processing, providing a route to high throughput, low-cost manufacturing. The metamaterial sandwich structure can be considered to consist of two "meta" elements. The Au layer is an optical element which controls and sculpts the flow of EM fields whilst the PZT is an electromechanical element, the response of which is amplified by its nanostructured properties.

Flexoelectricity is a generic property which all insulators display to varying degrees: they polarize on application to an inhomogeneous stress.[22] Conversely, the application of a nonuniform electric field gradient will result in stress. Flexoelectricity is closely related to piezoelectricity, also relying on symmetry breaking. However, in flexoelectricity, the breaking of the center of symmetry is the result of the perturbation of a nonuniform strain, rather than an intrinsic structural property. Consequently, flexoelectric effects are formally allowed in all materials irrespective of crystallinity or structure.

For an amorphous material in which piezoelectric effects can be neglected the inverse flexoelectric is mathematically expressed as[22]

$$\sigma = \mu \nabla E \tag{1}$$

where $\sigma$ is mechanical stress (defined by force per unit area), $E$ is the electric field, and $\mu$ is a (fourth order) flexoelectric tensor. The strain (i.e., % change in volume) is linearly dependent on the flexoelectric stress (within the elastic regime of the material) and thus $\nabla E$. This contrasts with the piezoelectric effect which is linearly dependent on $E$. Consequently, while flexoelectric effects may be minor in bulk samples, they will be significantly enhanced in nanostructured materials which can sustain large electric field gradients.[23–25] It is this enhancement which is at the heart of the observation we present.

The nanostructured polycarbonate substrates used in the study have been described in detail in previous studies.[19,26] The polymer substrates have areas ($500 \times 500\ \mu m^2$) of chiral "shuriken"-shaped indentations, shown in **Figure 1**A with either left-handed (LH) or right-handed (RH) sixfold rotational symmetry arranged in a square lattice. These nanoscale indentations have a depth of ≈80 nm, are 530 nm in diameter from arm to arm, and have a pitch of 700 nm. After an appropriate cleaning procedure (see Experimental Section) the polycarbonate substrates are deposited initially with a 20 nm layer of Pt. Subsequently, a PZT layer of thickness $X$ nm (where $X = (50/150)$ nm) is deposited using pulsed laser deposition (PLD), Figure 1B. These values were chosen because they provide examples of films which are thinner (50 nm) and thicker (150 nm) than the depth of the nanostructure indentations (80 nm). When the film is thinner than the depth of the indentation the PZT layers on the top surface of and within the indentation do not overlap directly, which could affect the stability of the device. Electron diffraction, Figure 1D,E, confirms that the PLD deposited PZT films display no long-range order, consistent with previous studies.[27] Finally, the sandwich structure is completed by the deposition of a ≈70 nm-thick Au film.

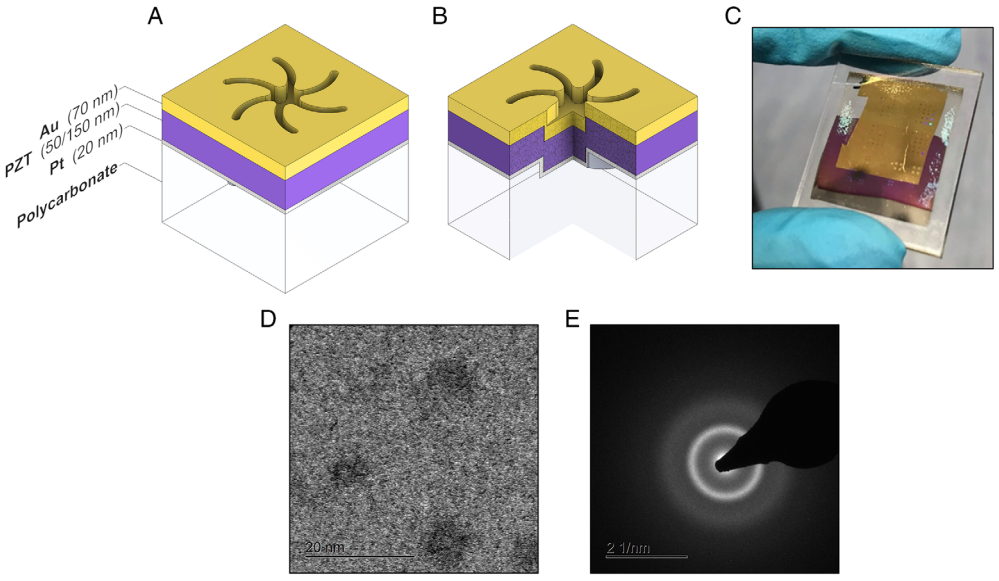


**Figure 1.** A) A schematic diagram of the device shows the platinum, PZT, and gold layers in a sandwich formation. B) Cross-sectional view of the indentations shows the distribution of each material. The thickness of the PZT layer is either 50 or 150 nm. C) A photograph of an actual 150 nm PZT metafilm is shown. D) Transmission electron microscopy of an as-deposited PZT film lacks the interference fringes that are characteristic of crystalline material. E) A selected area electron diffraction pattern similarly lack sharp diffractive features. The film is amorphous.

A photograph of the final device is shown in Figure 1C. The Pt and Au films act as electrodes between which a direct current (DC) voltage is applied. The resistance between the electrodes was >10 MΩ for all the metafilms studied, with <0.1 μA of current being drawn when the voltage was applied, and there was no evidence for dielectric breakdown or short circuits between the electrodes up to 12 V. However, for application of voltages >12 V, breakdown of the device was observed (see Supporting Information).

## 2. Results

### 2.1. Spectroscopic Measurements

To aid comparison, only data for LH structures will be presented, although qualitatively similar effects are observed for RH structure (see Supporting Information). Two types of optical spectra were collected from the devices: reflectance and optical rotatory dispersion (ORD). Reflectance spectra monitored the amount of linearly polarized light scattered from the shuriken structures relative to an unstructured Au film. ORD spectra show the amount of rotation of incident linearly polarized light as a function of wavelength. Due to the chirality of the shuriken structures, they rotate the plane of polarization of incident light. As expected, LH and RH nanostructures give otherwise identical mirror image ORD spectra. Both the 50 and 150 nm PZT devices produced similar reflectance and ORD spectra, which were not significantly different from those obtained previously from solely 70 nm-thick Au films deposited on the substrates.[19] Fundamental to this study is that ORD spectra are sensitive to the dimensions of the chiral shuriken structure. The ORD spectra, **Figure 2**, display a "bisignate" line shape which is characteristic of the chiroptical properties of the metamaterial, being described by a helical oscillator model.[19] The reflectance spectra, Figure 2, display a resonance which has a "dip" of enhanced reflectivity. This behavior has been observed in other metamaterials and has previously been referred to as plasmonic-induced reflectance/transparency (PIR/PIT).[26,28] In the present case, the PIR behavior has been attributed to the coupling mediated via near fields of optical bright and dark modes[26,29,30] (see Supporting Information). The similarities between the spectra, specifically the bisignate line shapes and peak-to-peak heights, collected from these metafilms and those of the plain Au equivalents suggest that the presence of the additional layers does not significantly degrade the structure of the shuriken indentation, which is supported by electron microscopy (see Supporting Information).

To assess the reproducibility of the voltage response, two devices where the PZT thickness, $X = 150$ nm were studied. We refer to these two samples as d150a and d150b. The optical properties of both devices have qualitatively similar dependencies on applied voltages. To aid clarity and reduce repetition only results for d150a will be presented here, analogous results for d150b can be found in Supporting Information. In both cases, there is a threshold voltage for changes in optical properties to occur, 12 and 10 V, respectively, for d150a and d150b.

The devices underwent up to 8 cycles in which they were maintained at the threshold voltages for a sufficient time-period for any change in optical properties to have stabilized. Subsequently, to complete the cycle, the device was earthed, whereupon the optical properties of the device gradually returned to those of the initial state after a period of <2 h (see Supporting Information for relaxation data). The relatively long relaxation period indicates that the observed changes in optical properties are not associated with capacitance effects. Maintaining a device at the threshold voltage resulted in a progressive decrease in the peak-to-peak magnitude of the bisignate ORD resonance until

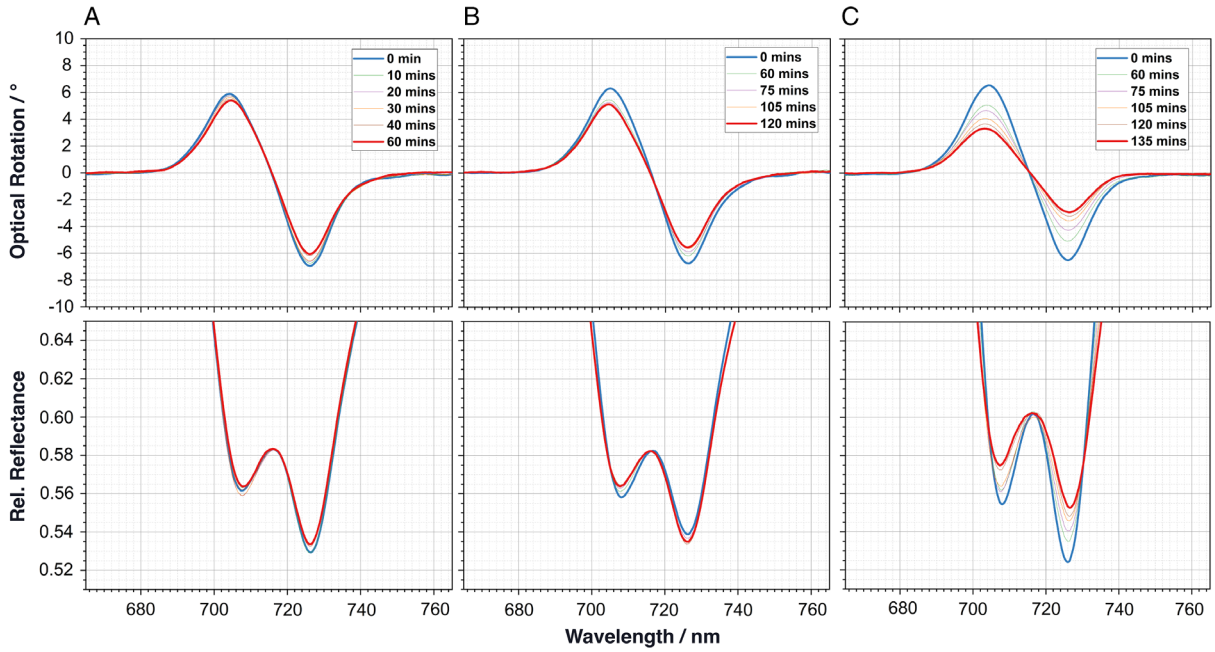


**Figure 2.** ORD (upper panels) and reflectance (lower panels) spectra of sample d150a maintained at the threshold voltage after A) one, B) four, and C) eight cycles. The time the spectra were collected after application of the voltage is given in the insets.

the value stabilized and a plateau region was achieved: see Figure 2A–C. With increasing number of cycles at the threshold voltage, stabilization of the ORD occurred at progressively lower peak-to-peak values, with a reduction to 47% of the initial value achieved after 8 cycles. The changes in the reflectance data, Figure 2A–C, follow a similar trend to the ORD data, however the spectral changes are less pronounced, with only significant changes, $\leq$4%, being observed after 8 cycles. The change in reflectance spectra is consistent with those arising from slight changes in magnitude and phase of coupling between the bright and the dark modes of the shuriken structure.[26] This interpretation is based on a simple classical coupled oscillator model of the plasmonic response of the Au nanostructure. This model includes the relative phases of the excitation of the dark and bright modes of the shuriken structure, and has been shown to replicate the shuriken reflectance spectra.[29] Thus, although the changes in coupling produce only small changes to the reflectance properties of the film they give rise to significantly greater changes in the chiroptical properties.

The device with a PZT thickness of 50 nm, subsequently referred to as d50a, also displays a threshold voltage, 18 V, for changes to the ORD, **Figure 3**A, and reflectance, Figure 3B, spectra. There is a reduction in the magnitude of the ORD resonance, which is smaller than changes observed for d150a and d150b. In a significant difference to the thicker PZT layer, the changes in the optical properties of d50a are irreversible. Scanning electron microscope (SEM) images, **Figure 4**, were collected pre- and post-application of the voltages. The micrographs appear to show a narrowing of both the arms and diameter of the central region of the shuriken structure, thus correlating the changes in spectroscopic response to structural modifications. From the SEM images, characteristic distances associated with the lateral dimensions of the nanostructures were determined, **Table 1**. It should be noted that SEM images can be distorted by aberration and charging effects. Thus, to unambiguously validate the proposed correlation between the changes in ORD response and structure requires additional evidence provided by numerical modeling, which will be presented in subsequent sections (also see Supporting Information for additional simulation data).

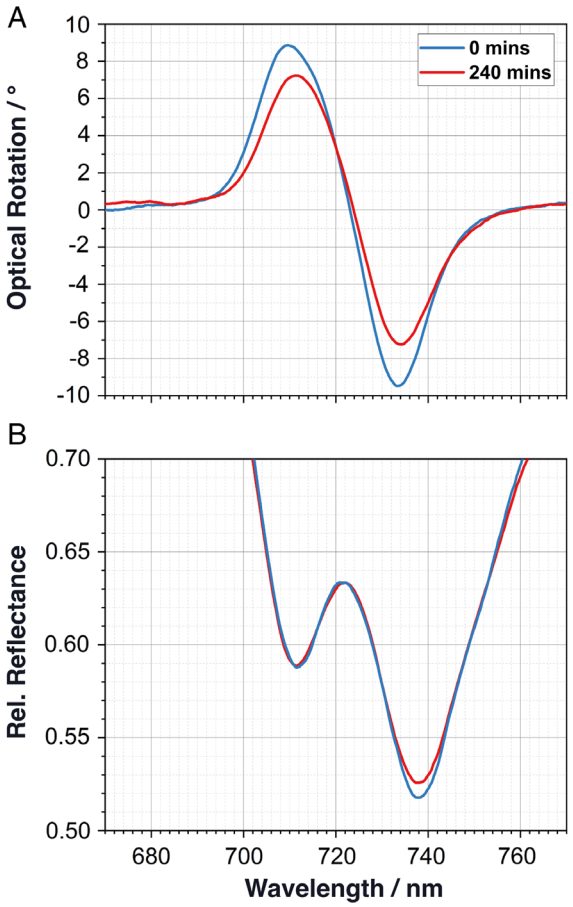


**Figure 3.** A) ORD and B) relative reflectance spectra for sample d50a before any voltage has been applied (blue) and after a voltage has been applied (red) and the plateau region has been attained.

## 2.2. Numerical EM Modeling

### *2.2.1. Electric Fields*

To facilitate understanding of the origins of the physical changes suggested by the data, the intensities and gradients of electric field distributions within the unperturbed sandwich structure have been calculated using numerical simulations, **Figure 5**. These simulation results support the hypothesis that the voltage-induced changes in the shuriken structure have arisen form the inverse flexoelectric effect. The field plots show that there are large field gradients at the base of the shuriken, Figure 5A,B and the side walls of the arms Figure 5C. However, at the top surface, 5 nm below the Au layer, the electric fields do not have significant gradients parallel or normal to the plane of the metafilm, Figure 5D. The location of the planes which contain the electric fields plots in Figure 5 are shown in Supporting Information. This spatial distribution of electric field gradients would result in inverse flexoelectric expansions which are consistent with the changes in physical structure. It should be noted that the electric field gradients are spatially varying. In the case of the base plane, they have larger magnitudes within the arms than in the central region. This suggests that a flexoelectric-induced expansion of the base would be nonuniform, with a greater reduction in depth at the arm than at the central region of the shuriken structures.

### *2.2.2. Spectroscopy Simulations*

Numerical simulations have also been used to qualitatively correlate experimental changes in ORD spectra to physical changes in structure. In contrast to the electric field simulations, computational constraints required that simplified structural models were used to replicate optical spectra. The two simplifications were that the PZT and Pt layers were not included and changes in shuriken dimensions were uniform across individual internal surfaces (i.e., base or side walls). Given that the thickness of the metafilm is significantly larger than the skin depth of Au at optical frequencies the nature of the environment underneath the film will not significantly affect the optical properties. The model structures used to replicate spectra are shown in **Figure 6**.

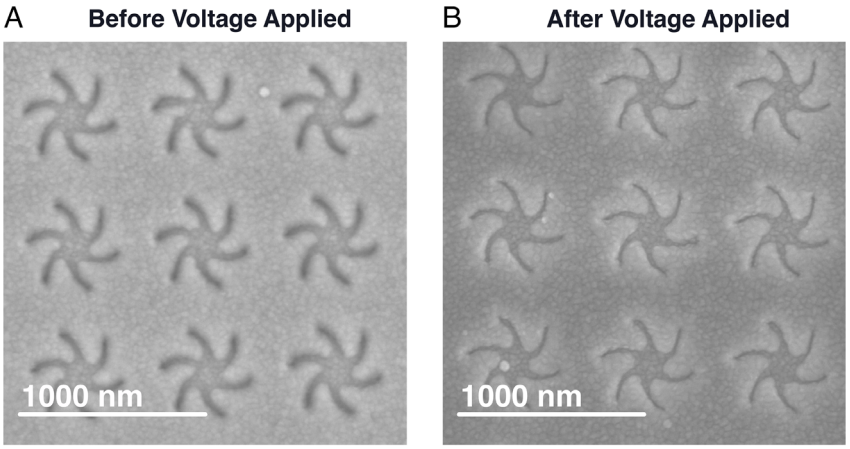


**Figure 4.** SEM images of sample d50a A) before and B) after the application of voltages show changes to the shuriken structure including narrowing of the arm widths.

**Table 1.** We parameterize the lateral geometric components of sample d50a of the nanostructure from SEM images captured before and after the threshold voltage was applied. The arithmetic mean of between 12 and 24 measurements is shown, along with their associated standard deviation ($\sigma$). These measurements are used for the construction of EM simulations. $p$ values are also given. Only the arm–arm separation shows no significant change.

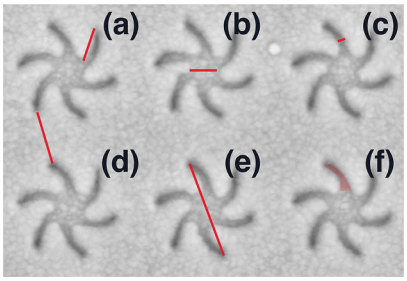


| | Before voltage applied | | After voltage applied | | p value |
|---|---|---|---|---|---|
| | Mean | $\sigma$ | Mean | $\sigma$ | |
| (a) Arm length [nm] | 173.0 | 11.9 | 166.0 | 9.2 | 0.012 |
| (b) Center diameter [nm] | 184.0 | 11.5 | 169.0 | 15.1 | 0.016 |
| (c) Arm width [nm] | 34.6 | 2.92 | 22.9 | 5.0 | $7.06 \times 10^{-12}$ |
| (d) Arm–arm [nm] | 314.0 | 12.6 | 309.0 | 10.2 | 0.445 |
| (e) Structure diameter [nm] | 521.0 | 7.4 | 505.0 | 6.2 | $9.16 \times 10^{-6}$ |
| (f) Arm area [nm$^2$] | 7840.0 | 878.0 | 5560.0 | 616.0 | $8.37 \times 10^{-7}$ |

Although utilizing simplified models, the simulations provide qualitative agreement with experimental data. In the first instance, the simulations were used to connect the SEM and spectroscopic data for the d50a device. The structural information provided by the SEM provided the lateral dimensions for the model. The structural parameters used to simulate the ORD spectra, **Figure 7**, pre- and post-application of voltage are shown in **Table 2**. The simulations qualitatively replicate the experimental results, specifically the reduction in the peak-to-peak height of the bisignate lineshape. This agreement between experiment and simulation could only be achieved if an expansion of the base (i.e., decrease in depth) comparable to the experimental observed lateral expansion of the side walls was included. Without this expansion of the base, simulations reveal a significant quenching of the level of the ORD signal (see Supporting Information).

Useable SEM images could not be obtained for the 150 nm PZT devices while they were being held at the operating voltages. Therefore, given the relatively short time scale, $\leq$2 h, of the relaxation of voltage-induced changes to ORD for the 150 nm PZT devices, SEM could not be used to monitor the associated structural changes. Consequently, the voltage-induced structural changes are inferred from simulating the experimental ORD spectra. It was assumed that qualitatively similar structural changes to that observed for the d50a. The parameters used to replicate the reduction in the ORD signal are shown in Table 2, and the simulated spectra are shown in Figure 7. The simulation shows a greater increase in the separation of the maxima and minima of the bisignate than is observed experimentally. We in part attribute such differences to the fact that the nonuniform expansion of the base implied by the modeling of the electric field gradients was not included in the model.

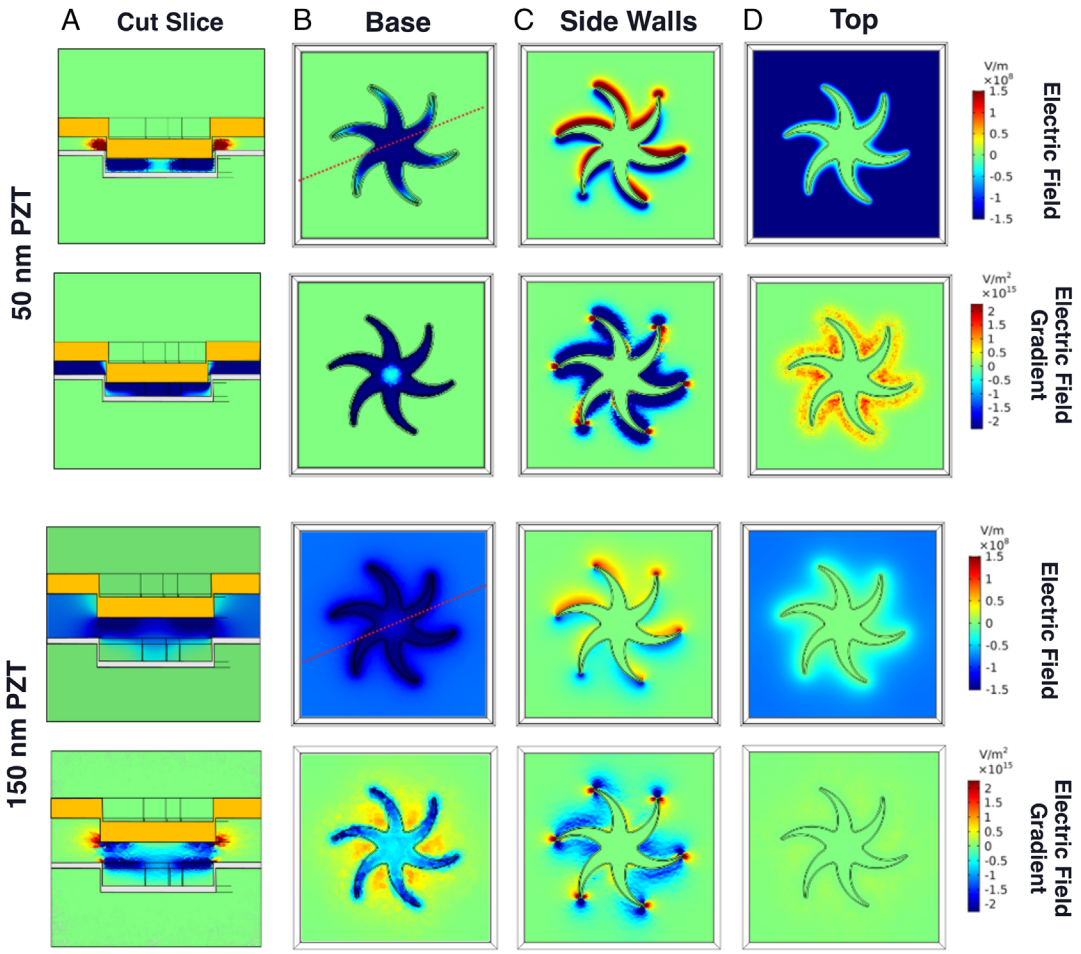


**Figure 5.** Electric field and electric field gradient plots of PZT material for the 50 (upper panels) and 150 (lower panels) nm thick structures. A) Electric field and electric field gradients (both *z*-components) for a plane cutting the nanostructure at the point marked by the dashed line in (B). B) Electric field and electric field gradient (*z*-components) at the base of the nanostructure. C) Electric field and electric field gradient (*y*-components) surrounding the arms of the nanostructure. The slice is taken halfway between the top and bottom surfaces. D) Electric field and electric field gradients (*z*-component) for the top surface of the PZT, 5 nm below the gold layer.

What is readily apparent from the simulated spectra is that only further slight, 1–2 nm, expansions of the wall and the base cause a significant decrease in the level of ORD.

## 3. Discussion

When combined, experimental and simulation data are consistent with the control of optical properties being due to structural changes originating from a significant flexoelectric, rather than a piezoelectric, response. The outward expansions of the internal surfaces of the shuriken required for simulations to replicate experimental data occur in areas with high electric field gradients rather than high electric field intensities. Consequently, there is a preferential expansion of the base leading to a decrease in the depth of the shuriken. The electric field intensities within the PZT in the regions of the base and top surfaces are similar. Thus, a piezoelectric response would expand both these identically thick base and top layers by the same amount, resulting in no change in the depth of the shuriken.

A more quantitative interpretation of the electromechanical control of chiroptical properties requires an understanding of the stress–strain response of the Au film. Using the electric field gradients derived from the numerical simulations and an estimate of $\mu$, the order of magnitude of the stress generated by the PZT layer can be determined using Equation (1). From previous work on PZT films $\approx 1 \times 10^{-6}\,\mathrm{cm}^{-1}$ is a reasonable estimate for the value of $\mu$ for the amorphous layer.[31] Materials with high dielectric constants, such has PZT, have larger $\mu$[32] than the $\approx 1 \times 10^{-10}\,\mathrm{cm}^{-1}$ typically expected for other materials.[33] From the simulations of the electric field gradients of the 150 nm PZT metafilms, Figure 5, there are localized areas of the walls of the arms and the base of the shurikens which have electric fields gradients $\approx 1 \times 10^{-16}\,\mathrm{Vm}^{-2}$. This would indicate that in localized regions, the internal surfaces of the shuriken experience stresses of the order of $\approx 10^{10}\,\mathrm{Nm}^{-2}$ at 12 V. This

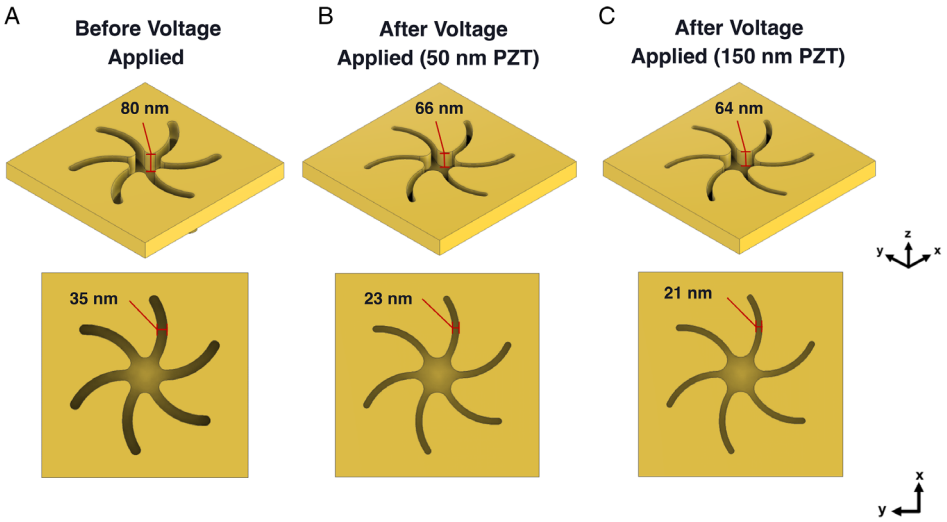


**Figure 6.** Idealized models used in simulations of ORD spectra shown in Figure 7, before (A) and after (B,C) the voltages are applied for 50 and 150 nm PZT, respectively. The positions of the *x*, *y*, and *z* axes are shown. ORD spectra are collected/simulated with the incident linear polarization parallel to the *x*-axis.

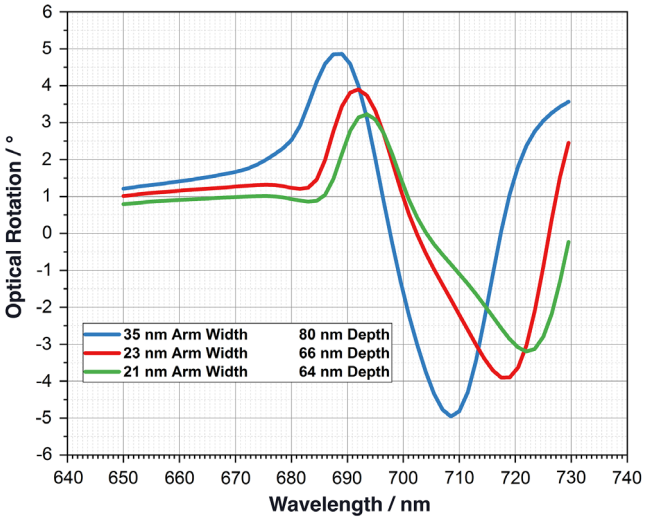


**Figure 7.** Simulated ORD spectra derived from models with structural parameters listed in Table 2. The blue spectrum corresponds to the structure before the application of voltage. The red spectrum corresponds to that obtained for the 50 nm PZT metafilm case. The green spectrum replicates a spectrum obtained for the 150 nm PZT metafilm.

value is comparable with the Young's modulus measured previously for 100 nm-thick Au films[34,35] of $\approx 6 \times 10^{10}$ Nm$^{-2}$. This indicates that the stresses produced by the inverse flexoelectric effect in PZT would be sufficient to deform the Au shuriken indentation, to produce the changes in volume implied by the experimental data and numerical modeling.

The apparent threshold for the voltage-induced optical changes and the dependency of the effect on the number of cycles can be rationalized with the known stress–strain relationships for Au films.[34,36] The stress–strain curves for Au nanofilms are complex, displaying an initial linear elastic phase for strains $\leq$1%, followed by a plastic regime in which greater deformations are induced for smaller increases in stress. Given that the change in volume of the shuriken are $\approx$10%, this implies that the required deformations of the Au films are in the plastic regime. It should be noted that assuming the Au film remains attached to the PZT layer, it will be restored to its initial position once relaxation is complete. To a first approximation, the stress induced in the metafilm layers will scale linearly with applied voltages and change in the ORD signal will correlate to strain (amount of deformation). Consequently, the stress–strain curve of the composite metafilm will have the same form as the voltage–ORD intensity curve. The effects of the number of voltage cycles can also be understood in terms of the mechanical behavior of the composite metafilm. Previous work has shown that the stress–strain behavior of Au films changes with multiple cycles of deformations.[34–36] With increasing cycles, the stress–strain curve moves to the right, i.e., it becomes progressively easier to deform the Au films. These changes in response are associated with physical alterations to the microstructure of the Au films.[36] This behavior would be consistent with the shorter timescales observed for changes in ORD signal with increasing number of cycles.

A remaining issue for discussion is the reversible versus irreversible behavior of devices with 50 and 150 nm PZT layers. The fundamental difference between the two composites is that in the 50 nm case, the PZT layer is thinner than the depth of the shuriken indentation (80 nm). Consequently, the layers of PZT on the top surface of the substrate and bottom of the indentation do not directly overlap. It is proposed that these two layers are connected via a thin composite layer covering the side wall of the shuriken indentation. Thus, it is suggested that this thinner side wall fractures under the stresses produced by the PZT layer, causing a "freezing-in" of the deformation.

Active chiral metamaterials capable of modulating chiroptical properties have been demonstrated, but are reliant upon complex

**Table 2.** We parameterize the dimension of the three shuriken nanostructure models used to simulate the ORD spectra shown in Figure 7. The parameters which significantly affect the ORD magnitude and to which the largest changes are made are (c) arm width and (g) indentation depth.

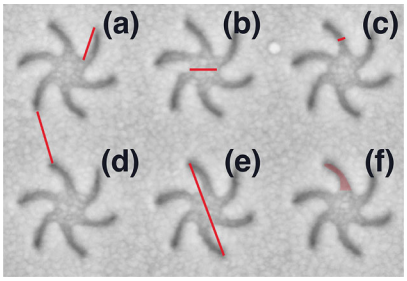


| | Before voltage applied | After voltage applied [50 nm thick] | After voltage applied [150 nm thick] |
|---|---|---|---|
| (a) Arm length [nm] | 185 | 185 | 185 |
| (b) Center diameter [nm] | 165 | 165 | 165 |
| (c) Arm width [nm] | 35 | 23 | 21 |
| (d) Arm–arm [nm] | 294 | 294 | 294 |
| (e) Structure diameter [nm] | 530 | 530 | 530 |
| (f) Arm area [$nm^2$] | 7820 | 5052 | 4617 |
| (g) Indentation depth [nm] | 80 | 66 | 64 |

multistep fabrication techniques,[37,38] or the introduction of external reagents[39,40] whose mechanism is more conducive toward chemical sensing applications. The dynamic range for polarization manipulation of these devices is $\leq 4^\circ$. Another configuration in the optical regime shows intensity-dependent changes equivalent to variations of optical rotation $\leq 0.1^\circ$.[41] Hence, the performance of the flexoelectric-based disposable metadevices, dynamic range of $\approx 4^\circ$, is comparable to the current state-of-the art.

## 4. Conclusion

This work is a proof-of-concept demonstration of a new paradigm of nanoelectromechanical control: the use of the inverse flexoelectric effect to manipulate the form factor of a nanostructure. The performance of the prototype device has not been optimized and could be improved. For instance, the slow and history-dependent response, likely to be associated with the mechanical properties of PZT layer, could be mitigated by using a more malleable flexoelectric polymer such as those based on polyvinylidene fluoride.[42] Also, a more substantial and reversible deformation may be possible if simpler 2D chiral arrangements of closely coupled dot indentations were used instead of the complex shuriken design. The concept of using flexoelectric materials to achieve nanoelectromechanical control has unique benefits. Specifically, the concept is convergent with high throughput polymer-based nanofabrication technologies such as injection moulding or nanoimprint lithography. Using an established platform of mass-produced prefabricated nanostructured polymer templates, active metadevices can be created through the room temperature deposition of sandwich layers. This process is analogous to that used to manufacture optical storage disks (compact discs (CDs), digital versatile discs (DVDs), and Blu-rays disks). Hence, this work provides a strategy for the low-cost fabrication of electromechanically controlled metamaterial elements for optoelectronic devices.

## 5. Experimental Section

*Fabrication*: The fabrication technique was described by Gadegaard et al.[43] The master shim was made using electron beam lithography. To create the master, 100 nm of poly(methyl methacrylate) resist was spin coated onto a Si wafer and baked for an hour at 180 °C. The resist was patterned using a VB6 UHR EWF lithography tool (Raith). The exposed resist was developed in isopropyl alcohol (IPA) and methyl isobutyl ketone, MIBK (3:1 ratio) for 60 s, then rinsed in copious amounts of IPA before dried in a stream of nitrogen gas. The shim for injection moulding was prepared by electroplating from the patterned resist master. The polycarbonate samples were created via an injection moulder using the nickel shim. The resulting nanostructured polycarbonate sample was cleaned in IPA and dried under a stream of $N_2$. A 20 nm platinum layer was then thermally evaporated onto the substrate.

PZT films were deposited by PLD using sintered PZT targets (Pi Kem Ltd., UK) in 50 mTorr pressure of oxygen. Deposition was conducted at room temperature directly onto structured polycarbonate substrates in a Neocera Pioneer PLD vacuum system, using a Coherent Compex Pro KrF excimer laser (248 nm, 20 ns pulses, 18 Hz, up to 200 mJ pulse energy). The target was rotated during deposition to minimize the transfer of particulates to the sample. The film structure was then characterized by transmission electron microscopy by depositing a $\approx 40$ nm-thick film directly onto an amorphous holey carbon film and imaged in a JEOL ARM CFEG instrument operated at 200 kV. Finally, 70 nm of gold was thermally evaporated onto the substrate.

*SEM Image Analysis*: The first measurement that was taken for each sample was an SEM image after manufacture, and the lateral dimensions shown in Table 1 were measured using the ImageJ image processing program. Twelve measurements were taken and averaged across multiple structures for the central diameter, arm-to-arm separation, arm area and structure diameter, and 24 were averaged for the arm width and length measurements. Probability ($p$) values[44] which parametrized the significance of differences between values before and after the application of voltages were calculated. $p$ Values $<0.04$ were indicative of a significant difference.

*EM Simulations*: EM simulations were carried out using a commercial finite-element package, COMSOL Version 5.5. Optical simulations were carried out using the Wave Optics module. The nanostructure array was simulated using periodic boundary conditions. Perfectly matched layer conditions were used above and below the input and output ports. The light incident upon the nanostructures was linearly polarized.

ORD was determined by calculation of the Stokes polarization parameters, the observables of the polarized field. Reflectance was determined by calculating the ratio of incident power reflected back onto a surface above the nanostructure array. Electric field simulations were carried out using the Electric Fields and Currents module. An electric potential equal to the threshold voltage was applied between the gold and platinum layers of the device. Electric field and electric field gradients were subsequently calculated at planes which bisected the shuriken nanostructure (see Supporting Information).

*Voltage-Dependent Measurements*: Sequentially larger DC voltages in the range 0–12 V were applied to the devices for a period of at least 1 h. The Au and Pt layers were the positive and negative electrodes, respectively. Both reflectance and ORD data were collected to monitor change in optical properties induced by the applied voltage. If no change in optical spectra was observed within this period, the voltage was increased. However, if changes were observed then the device was maintained at the voltage for a time period sufficient for spectra to stabilize and no further changes to occur. After this point, the device was maintained at 0 V and spectra collected to monitor any relaxation back toward the initial optical state of the device for periods of up to 3 h. This cycle was then repeated ≈15 h later.

## Supporting Information

Supporting Information is available from the Wiley Online Library or from the author.

## Acknowledgements

The authors acknowledge financial support from the Engineering and Physical Sciences Research Council (EP/P00086X/1 and EP/M024423/1) Technical support from the James Watt Nanofabrication Centre (JWNC). C.G. work was supported by the EPSRC CDT in Intelligent Sensing and Measurement, Grant Number EP/L016753/1. M.K. acknowledges the Leverhulme Trust for the award of a Research Fellowship.

## Conflict of Interest

The authors declare no conflict of interest.

## Keywords

active metamaterials, chirality, electromechanical, flexoelectrics

Received: September 9, 2020
Revised: October 5, 2020
Published online: December 2, 2020

[1] J. B. Pendry, A. Aubry, D. R. Smith, S. A. Maier, *Science* **2012**, *337*, 549.
[2] N. I. Zheludev, Y. S. Kivshar, *Nat. Mater.* **2012**, *11*, 917.
[3] M. Kauranen, A. V. Zayats, *Nat. Photonics* **2012**, *6*, 737.
[4] N. N. Jiang, X. L. Zhuo, J. F. Wang, *Chem. Rev.* **2018**, *118*, 3054.
[5] M. Wuttig, H. Bhaskaran, T. Taubner, *Nat. Photonics* **2017**, *11*, 465.
[6] S. Aksu, M. Huang, A. Artar, A. A. Yanik, S. Selvarasah, M. R. Dokmeci, H. Altug, *Adv. Mater.* **2011**, *23*, 4422.
[7] N. I. Zheludev, E. Plum, *Nat. Nanotechnol.* **2016**, *11*, 16.
[8] J. Y. Ou, E. Plum, L. Jiang, N. I. Zheludev, *Nano Lett.* **2011**, *11*, 2142.
[9] J.-Y. Ou, E. Plum, J. Zhang, N. I. Zheludev, *Nat. Nanotechnol.* **2013**, *8*, 252.
[10] A. Nemati, Q. Wang, M. H. Hong, J. H. Teng, *Opto-Electron. Adv.* **2018**, *1*, 25.
[11] K. Chen, G. Razinskas, T. Feichtner, S. Grossmann, S. Christiansen, B. Hecht, *Nano Lett.* **2016**, *16*, 2680.
[12] H. S. Ee, R. Agarwal, *Nano Lett.* **2016**, *16*, 2818.
[13] P. Gutruf, C. J. Zou, W. Withayachumnankul, M. Bhaskaran, S. Sriram, C. Fumeaux, *ACS Nano* **2016**, *10*, 133.
[14] P. Q. Liu, I. J. Luxmoore, S. A. Mikhailov, N. A. Savostianova, F. Valmorra, J. Faist, G. R. Nash, *Nat. Commun.* **2015**, *6*, 8969.
[15] Q. K. Liu, Y. X. Cui, D. Gardner, X. Li, S. L. He, I. I. Smalyukh, *Nano Lett.* **2010**, *10*, 1347.
[16] T. Driscoll, S. Palit, M. M. Qazilbash, M. Brehm, F. Keilmann, B. G. Chae, S. J. Yun, H. T. Kim, S. Y. Cho, N. M. Jokerst, D. R. Smith, D. N. Basov, *Appl. Phys. Lett.* **2008**, *93*, 024101.
[17] X. Zhao, G. Duan, A. Li, C. Chen, X. Zhang, *Microsyst. Nanoeng.* **2019**, *5*, 5.
[18] L. M. Cox, A. M. Martinez, A. K. Blevins, N. Sowan, Y. F. Ding, C. N. Bowman, *Nano Today* **2020**, *31*, 22.
[19] A. S. Karimullah, C. Jack, R. Tullius, V. M. Rotello, G. Cooke, N. Gadegaard, L. D. Barron, M. Kadodwala, *Adv. Mater.* **2015**, *27*, 5610.
[20] A. K. Tagantsev, *Phys. Rev. B* **1986**, *34*, 5883.
[21] X. Q. Fang, J. X. Liu, V. Gupta, *Nanoscale* **2013**, *5*, 1716.
[22] P. Zubko, G. Catalan, A. K. Tagantsev, *Annual Review of Materials Research* (Ed: D. R. Clarke), Vol. *43*, **2013**, pp. 387–421.
[23] M. S. Majdoub, P. Sharma, T. Cagin, *Phys. Rev. B* **2008**, *77*, 125424.
[24] D. Lee, A. Yoon, S. Y. Jang, J. G. Yoon, J. S. Chung, M. Kim, J. F. Scott, T. W. Noh, *Phys. Rev. Lett.* **2011**, *107*, 057602.
[25] A. Abdollahi, N. Domingo, I. Arias, G. Catalan, *Nat. Commun.* **2019**, *10*, 1266.
[26] C. Kelly, L. K. Khorashad, N. Gadegaard, L. D. Barron, A. O. Govorov, A. S. Karimullah, M. Kadodwala, *ACS Photonics* **2018**, *5*, 535.
[27] T. J. Zhu, L. Lu, M. O. Lai, *Appl. Phys. A* **2005**, *81*, 701.
[28] P. Tassin, L. Zhang, R. K. Zhao, A. Jain, T. Koschny, C. M. Soukoulis, *Phys. Rev. Lett.* **2012**, *109*, 5.
[29] R. Tullius, G. W. Platt, L. Khosravi Khorashad, N. Gadegaard, A. J. Lapthorn, V. M. Rotello, G. Cooke, L. D. Barron, A. O. Govorov, A. S. Karimullah, M. Kadodwala, *ACS Nano* **2017**, *11*, 1203.
[30] C. Kelly, R. Tullius, A. J. Lapthorn, N. Gadegaard, G. Cooke, L. D. Barron, A. S. Karimullah, V. M. Rotello, M. Kadodwala, *J. Am. Chem. Soc.* **2018**, *140*, 8509.
[31] W. H. Ma, L. E. Cross, *Appl. Phys. Lett.* **2005**, *86*, 3.
[32] W. Ma, L. E. Cross, *Appl. Phys. Lett.* **2001**, *79*, 4420.
[33] S. M. Kogan, *Sov. Phys. Solid State* **1964**, *5*, 2069.
[34] B. Merle, M. Goeken, *J. Mater. Res.* **2014**, *29*, 267.
[35] A. S. Tran, T. H. Fang, J. W. Hsiao, *Curr. Appl. Phys.* **2019**, *19*, 332.
[36] R. D. Emery, G. L. Povirk, *Acta Mater.* **2003**, *51*, 2079.
[37] X. H. Yin, M. Schaferling, A. K. U. Michel, A. Tittl, M. Wuttig, T. Taubner, H. Giessen, *Nano Lett.* **2015**, *15*, 4255.
[38] A. Kuzyk, R. Schreiber, H. Zhang, A. O. Govorov, T. Liedl, N. Liu, *Nat. Mater.* **2014**, *13*, 862.
[39] Z. Wu, X. Chen, M. Wang, J. Dong, Y. Zheng, *ACS Nano* **2018**, *12*, 5030.
[40] Z. Wu, J. Li, X. Zhang, J. M. Redwing, Y. Zheng, *Adv. Mater.* **2019**, *31*, 1904132.
[41] S. P. Rodrigues, S. F. Lan, L. Kang, Y. H. Cui, P. W. Panuski, S. X., Wang, A. M. Urbas, W. S. Cai, *Nat. Commun.* **2017**, *8*, 8.
[42] J. Liu, Y. Zhou, X. P. Hu, B. J. Chu, *Appl. Phys. Lett.* **2018**, *112*, 4.
[43] N. Gadegaard, S. Mosler, N. B. Larsen, *Macromol. Mater. Eng.* **2003**, *288*, 76.
[44] M. Krzywinski, N. Altman, *Nat. Methods* **2013**, *10*, 1041.